Article

Miscible chemical ordering in Ti-Cr-Mo quinary system by solid solution of Mo$_2$Ti$_2$AlC$_3$ and Cr$_{2.5}$Ti$_{1.5}$AlC$_3$ o-MAXs
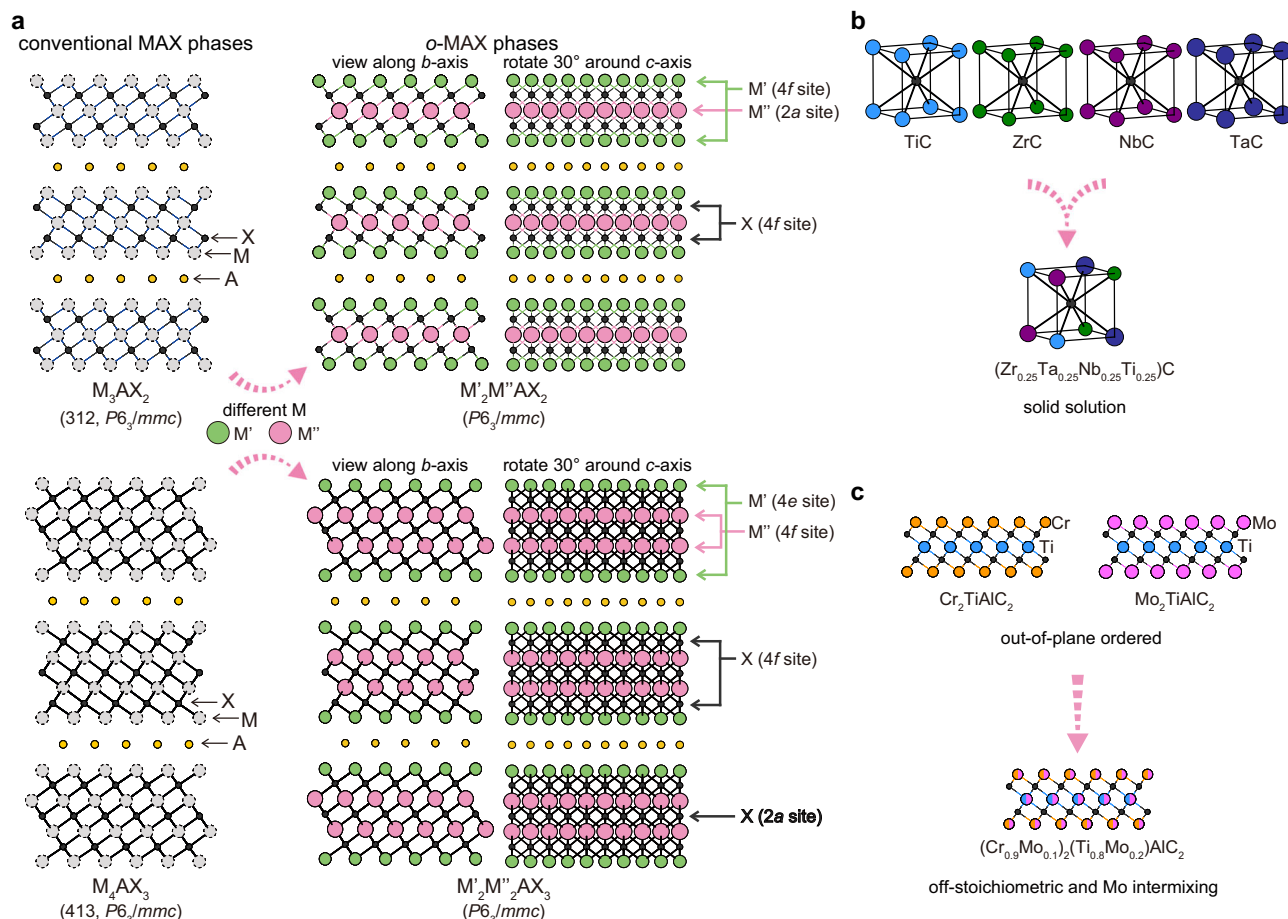
Cheng-Feng Du [image] ✉, Chuanchao Wang, Mengfei Xu, Yaqing Xue, Lili Xue, Conghui Meng, Long Wang, Weihong Qi ✉, Xuqing Liu & Hong Yu [image] ✉

Out-of-plane ordering is promising for separately adjusting the heterodesmic chemical bonding inside the MAX phase thus tuning their properties, while constructing the out-of-plane ordered-MAX (o-MAX) is still a challenge. In this work, a strategy towards o-MAX by solid solutions of two existing o-MAXs is verified, i.e., Cr$_{2.5}$Ti$_{1.5}$AlC$_3$ and Mo$_2$Ti$_2$AlC$_3$, with controllable stoichiometric ratios (1:2, 1:1, and 2:1). A miscible chemical ordering is observed in three Ti-Cr-Mo quinary MAXs, which inherits the out-of-plane ordering from both parental o-MAXs. Meanwhile, through density functional theory (DFT) calculations, the electronic structure and bonding states inside the quinary o-MAXs are analyzed. Based on the calculations, anisotropic and improved mechanical properties are predicted, which agree with the experimental observed high compressive strength and tunable capacity of energy dissipation. The present work proves a promising way for synthesizing multicomponent o-MAXs.

In recent decades, the pursuit of integrating advantages from both ceramics and alloys has been achieved in a unique nanolamellar material, namely, the MAX phase ceramic[1–3]. Structurally, the lattice of the MAX phase can be regarded as an alternative staking of the metal carbide/nitride slab (M$_{n+1}$X$_n$) extracted from the {111} plane of an fcc lattice, and the atomic layer of main group elements (A)[4,5]. Owning to the distinct chemical composition of the M$_{n+1}$X$_n$ slab and A layer, covalent bonds dominate the M$_{n+1}$X$_n$ slabs, whereas much weaker bonds consisting of covalent, metallic, and/or ionic interactions exist between the M$_{n+1}$X$_n$ and A layers[6,7]. Given the heterodesmic bonding characteristic, the MAX phase ceramics not only function as the structural material revealing excellent chemical inertness outdistancing alloys and machinability superior to most ceramics[8–12], but also act as precursors towards novel two-dimensional MXene materials in recent years[13–15]. More importantly, the diversified chemical composition endows the MAX tunable physicochemical properties, in which the effects can be extended to the MXene-derivates[16,17]. On the other hand, due to the highly anisotropic structure with distinct atomic distribution tendency, the composition-structure dependency is more complex in the MAX phase than that in alloys or simple ceramic

systems[18,19]. Therefore, although tremendous research efforts have been devoted to synthesizing new MAXs with different elemental combinations[20,21], predicting and controlling the structure of multi-component MAXs is still challenging.

Recently, a secondary chemical ordering, namely, the out-of-plane ordering of the M metals, has been experimentally and theoretically verified in high-level multicomponent MAX phases (n = 2 or 3)[21,22]. In brief, the thickened M$_{n+1}$X$_n$ slabs result in two kinds of layers (Wyckoff sites) for M atoms to reside, one is adjacent to the A layer, while the other one is solely surrounded by X atoms (Fig. 1a). Due to the different coordination environments of the two layers, preferential occupation of different M atoms (M′ and M″) occurs, thus leading to an ordered arrangement of every M″-layer sandwiched in between two M′-layers in the sub-lattice scale while maintaining the lattice symmetry (Fig. 1a)[23]. Given the distinct atomic arrangement, the MAXs with such out-of-plane ordering are defined as "o-MAX". Benefiting from the out-of-plane ordering, the M-A and M-X bonding can be regulated individually, which opens a new space for the performance-oriented designing of the MAXs and their derivates[24–26]. For example, by varying the composition of Ti$_3$AlC$_2$ to the Mo$_2$TiAlC$_2$ o-MAX, the

State Key Laboratory of Solidification Processing, Center of Advanced Lubrication and Seal Materials, Northwestern Polytechnical University, Xi'an, Shaanxi, PR China. ✉e-mail: cfdu@nwpu.edu.cn; qiwh216@nwpu.edu.cn; yh@nwpu.edu.cn

Fig. 1 | Lattice structure and properties of *o*-MAXs compared to conventional MAXs. a Schematic illustration of the out-of-plane ordering in M_3AX_2 (312) and M_4X_3 (413) MAX with two different metal planes. The orange and black spheres represent A and X atoms in the MAXs' lattice, respectively, whereas gray spheres represent homogeneous M atoms in the lattice. Green and pink spheres indicate M′ and M″ atoms in the *o*-MAXs' lattice, respectively. **b** Illustration of the solid solution of isomorphic *fcc* carbide lattice. **c** Illustration of the formation of an off-stoichiometric $(Cr_{0.9}Mo_{0.1})_2(Ti_{0.8}Mo_{0.2})AlC_2$ product from two 312 *o*-MAXs.

compressive strength nearly doubled while the fracture toughness remained unharmed[27]. Whereas by further thickening the $M_{n+1}X_n$ slabs, the $Mo_2Ti_2AlC_3$ presented a higher strength of 1145 MPa accompanying by an enhanced toughness[28]. As plotted in an Ashby map showing the toughness-strength relationship of reported MAX phases (Supplementary Fig. 1 and Supplementary Table 1)[27–44], the out-of-plane ordering has revealed distinct potential in improving the mechanical properties. However, due to the complex chemical composition and competition between multiple intermediates, the discovery of *o*-MAXs is rather sluggish and only limited *o*-MAXs have been experimentally synthesized heretofore[23]. Meanwhile, different from the solid solution of simple isomorphic lattice, *e.g.*, *fcc* carbides (Fig. 1b)[45], the blend of two *o*-MAXs usually leads to the destruction of their secondary chemical ordering. For example, Cr_2TiAlC_2 and Mo_2TiAlC_2 are two *o*-MAXs with strictly out-of-plane ordering[38,39], while when blending their lattice, only an off-stoichiometric product with Mo intermixing has been obtained (Fig. 1c)[46]. On account of the increasing complexity within the resulting multi-elemental system, the succession of chemical ordering from both parental *o*-MAXs is still hard to achieve, let alone establish the performance-oriented designing of this MAX subfamily.

In this work, three quinary *o*-MAXs are prepared by forming solid solutions from two *o*-MAX ($Cr_{2.5}Ti_{1.5}AlC_3$ and $Mo_2Ti_2AlC_3$) with three stoichiometric ratios (1:2, 1:1, and 2:1), namely, the $(Cr_{0.78}Mo_{0.22})_2(Ti_{0.87}Mo_{0.13})_2AlC_3$ (denoted as Mo_1Cr_2), $(Cr_{0.65}Mo_{0.35})_2(Ti_{0.88}Mo_{0.12})_2AlC_3$ (denoted as Mo_1Cr_1), and $(Cr_{0.52}Mo_{0.48})_2(Ti_{0.88}Mo_{0.12})_2AlC_3$ (denoted as Mo_2Cr_1), respectively. Unexpectedly, the out-of-plane ordering of both parental *o*-MAXs is inherited in the three quinary *o*-

MAXs. Density functional theory (DFT) calculations are performed to illuminate the electronic structure and chemical bonding characters of the new quinary *o*-MAX, which reveals an anisotropic and improved mechanical property. In agreement with the theoretical predictions, a high compressive strength (*i.e.*, 1456.7 ± 64.3 MPa) as well as tunable capacity of energy dissipation is achieved in the quinary *o*-MAXs. Given the interesting structure and the tunable properties, the present work proves a promising way for synthesizing *o*-MAXs with complex chemical composition and specific chemical ordering.

Results and discussions

Atomic resolution of out-of-plane ordering in the quinary *o*-MAXs

The high-purity bulks were obtained through a two-step stratagem, which includes a spark plasma sintering (SPS) followed by high-temperature annealing. Since a typical MAX phase is generated after the SPS step (Supplementary Fig. 2)[47], the element distribution with atomic resolution in the three MAXs was confirmed under a double-spherical aberration-corrected transmission electron microscope (ACTEM) via high-angle annular dark-field (HAADF) scanning transmission electron microscopy (STEM) mode. As shown in Fig. 2a, along the [11$\bar{2}$0] zone axis of Mo_1Cr_2, stacking of four-atomic-thick slabs is observed. Meanwhile, distinct enrichment of Al, Ti, and Cr atoms in different layers is confirmed by EDS mapping, which demonstrates the characteristic out-of-plane chemical ordering similar to that of $Mo_2Ti_2AlC_3$ and $Cr_{2.5}Ti_{1.5}AlC_3$[47,48]. Accordingly, EDS line profiles were acquired perpendicularly spanning multiple slabs (in yellow). As
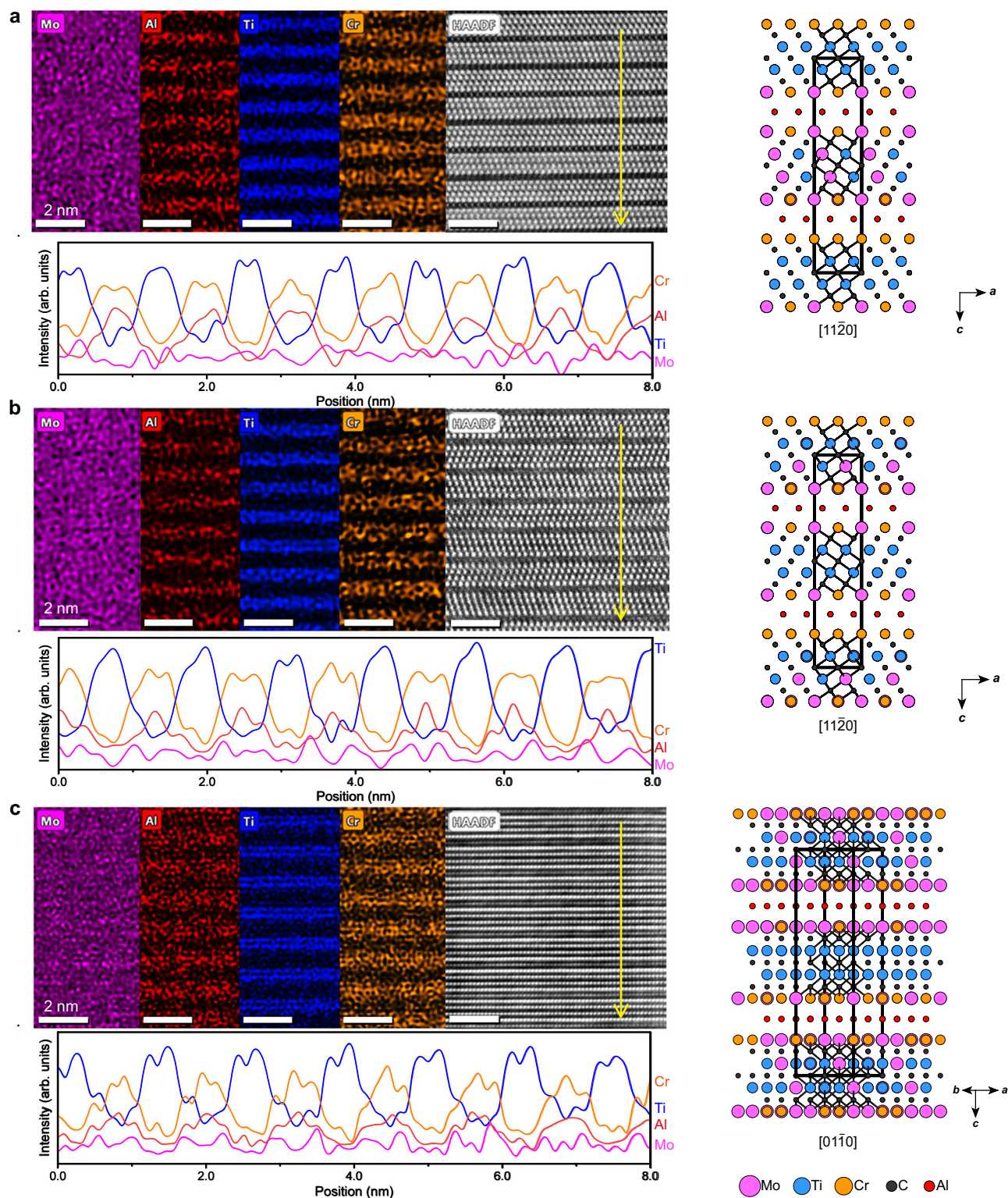
Fig. 2 | Atomic resolution of out-of-plane ordering in the quinary o-MAXs. Double Cs correction HAADF-STEM images, EDS mapping, corresponding line profile, and the crystal model showing the projection direction. **a** Mo_1Cr_2, **b** Mo_1Cr_1, and **c** Mo_2Cr_1. Line profiles are acquired along the respective yellow arrow and the HAADF signal of the lattice is shown as gray background. The orange, blue, pink, and red lines are corresponded to Cr, Ti, Mo, and Al, respectively. Source data are provided as a Source Data file.

plotted in Fig. 2a, Al layers are alternatively arranged in the interlaminar region of M_4C_3 slabs. Meanwhile, the distribution of Ti and Cr are clearly separated, corresponding to the $4f$ and $4e$ Wyckoff sites in the lattice, respectively. For the Mo atoms, a distribution in both $4f$ and $4e$ Wyckoff sites is shown. Figures 2b and 2c present the HAADF-STEM images and corresponding EDS results of Mo_1Cr_1 and Mo_2Cr_1, respectively. A similar distinct difference in the location of Ti and Cr in $4f$ and $4e$ Wyckoff sites can be confirmed, while the Mo atoms still distribute at both sites irrespective of their increased content. Moreover, it should be pointed out that in the two parental o-MAXs, a small
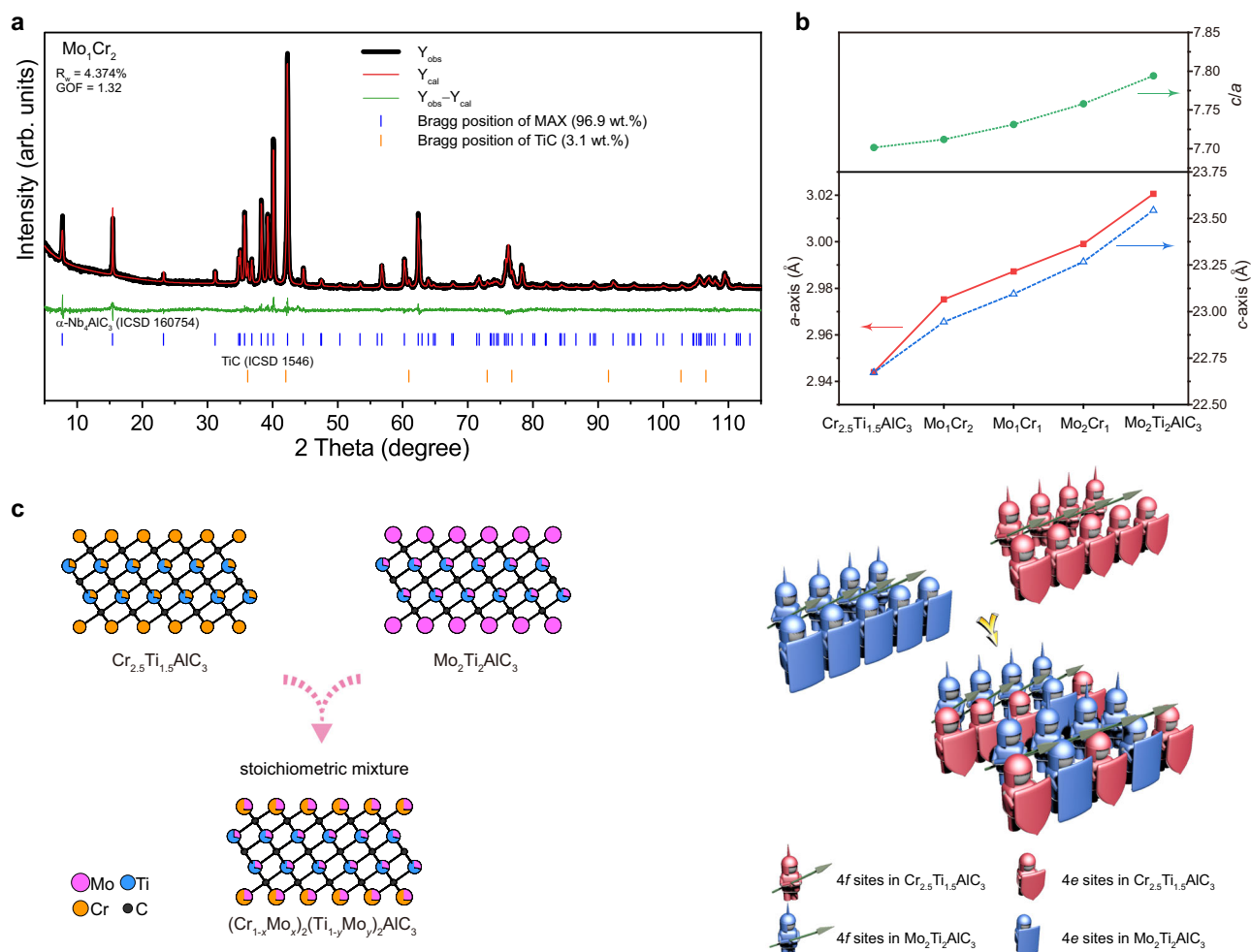
Fig. 3 | Phase structure of the quinary o-MAXs and schematic of the ordering inherits. a Rietveld refinement of XRD pattern for annealed Mo_1Cr_2 MAX. The diffraction patterns of MAX and TiC phase are derived from the standard crystallographic data of α-V_4AlC_3 (ICSD 160754) and TiC (ICSD 1546). **b** The change in lattice parameters of the three quinary o-MAXs compared to $Cr_{2.5}Ti_{1.5}AlC_3$ and $Mo_2Ti_2AlC_3$. The red and blue plots correspond to the parameters of a-axis and c-axis, respectively, whereas the green plot shows the c/a ratio. **c** Schematic illustration of the stoichiometric solid solution of $Cr_{2.5}Ti_{1.5}AlC_3$ and $Mo_2Ti_2AlC_3$ to form the quinary o-MAX and the succession of the out-of-plane ordering. The red and blue knight phalanxes refer to the lattice of $Cr_{2.5}Ti_{1.5}AlC_3$ and $Mo_2Ti_2AlC_3$, respectively, whereas the equipped shield and spear, respectively, represent the 4e and 4f metal sites in each o-MAX. Source data are provided as a Source Data file.

amount of metal intermixing between $4f$ and $4e$ sites was suspected as well[21,47,48]. However, due to the potential irradiation-induced atomic displacements[49,50], as well as the limitation of state-of-the-art apparatus, solid proof for such an intermixing is lacking so far. Therefore, pinpointing the atomic location in the three quinary o-MAXs might be left in the future.

Phase and structure of the quinary o-MAXs

Based on the X-ray diffraction (XRD) Rietveld refinements, the purity of the MAX phase is only around 75% just after SPS sintering. The crystallized impurities are mainly metal carbides for Mo_1Cr_2 (25.1 wt.%) and Mo_1Cr_1 (30.0 wt.%). Whereas metal carbides (19.0 wt%) accompanied by Al_2O_3 (4.3 wt.%) are detected in Mo_2Cr_1 (Supplementary Table 2). The elemental distribution in the as-sintered specimens was then acquired under a scanning electron microscope (SEM) with an energy-dispersive X-ray spectroscope (EDS). Through EDS mapping (Supplementary Fig. 3), an inhomogeneous distribution of Ti, Cr, and Al is detected in three specimens, which coincides with the possible impurities from XRD refinement. Further, EDS point analysis was performed based on backscattered-electron (BSE) analysis. As shown in Supplementary Fig. 4, bright lamellar grains on the as-sintered samples possess atomic compositions close to the chemical formula of the

corresponding MAX phase (Supplementary Table 3). Meanwhile, the gray granular regions can be identified as metal carbides. Given the complex composition of Ti, Mo, and Cr in the region, the carbides should be a solid solution as well. The distinct black particles can be ascribed to the alloy or Al_2O_3 species. The impurities in the as-sintered specimens can be ascribed to the competitive formation of multiple intermedia during SPS sintering. Therefore, further high-temperature annealing was applied to facilitate the transformation of these intermedia to the MAX phase.

The XRD Rietveld refinement results of the three annealed o-MAXs are shown in Fig. 3a and Supplementary Fig. 5, which demonstrate a high MAX phase purity of 96.9, 94.8, and 93.0 wt.% for Mo_1Cr_2, Mo_1Cr_1, and Mo_2Cr_1, respectively. The Mo_1Cr_2 ($R_{wp} = 4.374\%$) and Mo_1Cr_1 ($R_{wp} = 4.455\%$) present impurities of metal carbides, whereas metal carbides (5.0 wt.%) and Al_2O_3 (2.0 wt.%) are detected from Mo_2Cr_1 ($R_{wp} = 4.217\%$). The lattice parameters obtained from the refinement are summarized in Table 1 and plotted in Fig. 3b. For comparison, the reported lattice parameters of $Cr_{2.5}Ti_{1.5}AlC_3$ and $Mo_2Ti_2AlC_3$ are also included[47,48]. With an increasing Mo/Cr ratio, the length of the a-axis rises from 2.944 Å of $Cr_{2.5}Ti_{1.5}AlC_3$ to 2.975, 2.987, and 2.999 Å of Mo_1Cr_2, Mo_1Cr_1, and Mo_2Cr_1, respectively. Similarly, the length of the c-axis for the three o-MAXs reveals the same trend

Table 1 | XRD refinement results of the three o-MAXs

Lattice Parameters	Mo_1Cr_2	Mo_1Cr_1	Mo_2Cr_1
Crystal system	hexagonal	hexagonal	hexagonal
Space group	$P6_3/mmc$	$P6_3/mmc$	$P6_3/mmc$
a (Å)	2.97525	2.98721	2.99908
c (Å)	22.94493	23.09518	23.26694
V (Å³)	175.899	178.477	181.236
D_{cal} (g cm⁻³)	5.559	5.676	5.799
Atomic composition (4e)	Cr:0.7831 Mo:0.2169	Cr:0.6466 Mo:0.3534	Cr:0.5227 Mo:0.4773
Atomic composition (4f)	Ti:0.8693 Mo:0.1307	Ti:0.8794 Mo:0.1206	Ti:0.8783 Mo:0.1217
R_{wp} (%)	4.374	4.455	4.217
GOF	1.32	1.39	1.31

between the values of $Cr_{2.5}Ti_{1.5}AlC_3$ and $Mo_2Ti_2AlC_3$. The c/a ratio of the three quinary o-MAXs is in a range of 7.713–7.758, which is comparable to the conventional MAXs (Supplementary Table 4). Along with the increasing Mo/Cr ratio, expansion of the unit cell occurs, which demonstrates the formation of solid solutions of $Cr_{2.5}Ti_{1.5}AlC_3$ and $Mo_2Ti_2AlC_3$.

Additionally, given the distinct out-of-plane ordering of Ti, Cr, and Mo atoms observed from the atomic resolution HAADF-STEM images, Rietveld refinement was applied to confirm the occupation of Ti, Cr, and Mo in the 4e and 4f Wyckoff sites, as well as further estimating their proportion. As shown in Table 1, Cr andd Mo at the 4e sites while Ti and Mo co-occupying at the 4f sites in the quinary o-MAXs are physically feasible. Meanwhile, appending either Cr at the 4f site or Ti at the 4e site leads to a negative occupation of elements, which reflects physically impossible occupations. The experimental formulas from the XRD refinements match well with the starting elemental ratio of the three quinary o-MAXs, which demonstrates a stoichiometrically solid solution of $Cr_{2.5}Ti_{1.5}AlC_3$ and $Mo_2Ti_2AlC_3$ (Supplementary Table 5). Moreover, the increased Mo content mainly affects the atomic composition of the 4e site, whereas the Ti/Mo ratio in the 4f site is nearly constant. Given the similar intermixing phenomenon in the parental o-MAXs and nearly the same occupancy of the 4f site in $Mo_2Ti_2AlC_3$ ($Ti_{0.86}Mo_{0.14}$) as obtained in the three quinary o-MAXs[47,48], inheriting the out-of-plane ordering in the quinary o-MAXs by forming a solid solution of the two parental o-MAXs with a certain ratio of formula is reasonable (Fig. 3c).

The homogeneity of obtained specimens was confirmed by SEM. As acquired under low-magnification EDS mapping (Supplementary Fig. 6), all the annealed MAXs present a homogeneous distribution of Mo, Ti, Cr, Al, and C. Proved by the BSE image, the stacking of bright lamellar MAX grains gets denser after annealing, while the metal carbides nearly disappear (Supplementary Fig. 7). Meanwhile, from the corresponding EDS point analysis, the Ti content in the MAX grains increases after annealing (Supplementary Table 6), which also evidences the slow solid reaction of metal carbides with alloys to form the MAX phase. Moreover, the grain size of the three MAXs before and after annealing is measured according to the BSE images. The average lateral size of Mo_1Cr_2 is nearly constant after annealing (7.57 vs 7.69 μm). Whereas the grains of Mo_1Cr_1 and Mo_2Cr_1 slightly increase after annealing, which is 8.65 vs. 7.86 μm and 7.72 vs. 6.20 μm, respectively (Supplementary Fig. 8).

Bonding analyses of the out-of-plane ordered solid solution structure

To get an in-depth insight into the electronic structure of the quinary o-MAXs, the total density of states (TDOS) of the two parental o-MAXs and Mo_1Cr_1 are plotted together with their projected density of states (PDOS) of Mo, Cr, Ti, Al, and C near the Fermi level (E_f, Supplementary Figs. 9, 10)[51,52]. As shown in Fig. 4a–c, the E_f of the three compounds is dominated by the contribution from the d-d interaction of 4e metal

atoms, whereas the states at lower energy levels around −8.5 to −0.5 eV are ascribed to the d-p hybridizations between the transition metal and Al or C atoms[52]. Accordingly, the crystal orbital Hamilton population (COHP) analysis of the typical M-C and M-Al bonds was performed[53–55]. As shown by the −COHP plots, the Cr-C and Mo-C interactions below E_f are contributed by a majority of bonding orbitals with a small anti-bonding portion lying at −2.5 eV to E_f. While for the Ti-C interactions, the contribution from −8.5 eV to E_f is dominated by the bonding state.

For a more detailed understanding of the impacts of the solid solution of the two parental o-MAXs on bonding states in Mo_1Cr_1, −COHP and the integrated (−ICOHP) curves are examined. Figure 4d illustrates the coordination environments of the 4f Ti(14) atom with a neighboring Mo(1) atom. The Ti(14) atom connects to three 4f C atoms (C(16), C(20), and C(24)) and three 2a C atoms (C(1), C(3), and C(5)). As shown in Fig. 4e, f and Supplementary Figs. 11, the introduction of hetero Mo atom results in differentiated Ti-C bonds in Mo_1Cr_1 when compared to that of $Mo_2Ti_2AlC_3$ and $Cr_2Ti_2AlC_3$. Meanwhile, the Ti-C(4f) bonds in the three o-MAXs present mainly bonding states at and close to E_f, while the Ti-C(2a) bonds show crossover points of bonding and antibonding regions near E_f. Similar bonding states also have been reported in the 312 system[22]. As the 4f Ti and 2a C layers possess a more bulk-phase-like coordination environment within the thickened $M_{n+1}C_n$ layer, the near-zero COHP value close and at the E_f demonstrates limited energetic contribution from the Ti-C(2a) bonds[54]. Such −COHP curves also indicate higher covalency of the Ti-C(2a) bonds than the corresponding Ti-C(4f) bonds, which is in accordance with the higher −ICOHP values[56]. Bader charge analysis (Supplementary Tables 7, 8) was then performed to evaluate the overall charge transfer onto the adjacent C atoms[57]. A reduced charge gain on 2a C atoms in Mo_1Cr_1 is revealed when compared to that of $Mo_2Ti_2AlC_3$ and $Cr_2Ti_2AlC_3$, whereas the charge transfer onto 4f C atoms is relatively constant. As a result, the −ICOHP values of both Ti-C(2a) and Ti-C(4f) show an intermediate Ti-C bond strength in Mo_1Cr_1 in between the parental o-MAXs (Supplementary Table 9).

Meanwhile, populated antibonding states of the M(4e)-C(4f) bonds are detected at and close to E_f. However, based on the −ICOHP values, the solid solution of Cr and Mo atoms at the 4e sites in Mo_1Cr_1 weakens the Cr(4e)-C(4f) interactions while enhancing the Mo(4e)-C(4f) interactions when respectively compared to that of $Cr_2Ti_2AlC_3$ and $Mo_2Ti_2AlC_3$ (Fig. 5a–c, Supplementary Figs. 12a, b, and Supplementary Table 9). As demonstrated by the Bader charge analysis (Supplementary Tables 7, 8), the adjacent arrangement of Cr and Mo atoms at the 4e sites facilitates the charge donation of Cr while reducing the charge donation of Mo. Thus, the altered covalency of both M(4e)-C(4f) interactions in Mo_1Cr_1 leads to an evolution of bond strengths after forming a solid solution. Similarly, for the M(4e)-Al interactions in Mo_1Cr_1, enhanced Mo(4e)-Al interactions and weakened Cr(4e)-Al interactions are observed, which is consistent with the change in charge donation from the respective M(4e) and Al atoms comparing to that of the respective parental o-MAX (Fig. 5d, e and Supplementary Figs. 12c, d). Based on the Bader charge analysis (Supplementary Table 9), the 4e metal and Al atoms are all positively charged, which indicates a hybridization of valence electron or covalent bonding characters[58]. After forming a solid solution, the reduced charge donation might enhance the electron hybridization, and vice versa. Further, the average −ICOHP values of the corresponding bonds in the three o-MAXs and the normalized −ICOHP values based on their respective M(4e)-Al bond are plotted (Supplementary Figs. 13). As shown, although the M(4e)-Al bond is the weakest bond in the three o-MAXs, the strength of M-C bonds varies. The strongest bond is the Mo(4e)-C(4f) bond in $Mo_2Ti_2AlC_3$ while Ti(4f)-C(2a) bond in $Cr_2Ti_2AlC_3$. Moreover, the M(4f)-C(4f) bond is relatively weak in the two parental o-MAXs when compared to their strongest bond. On the contrary, after solid solution, the relative strength of M(4e)-C(4f), M(4f)-C(4f), and M(4f)-C(2a) bonds in Mo_1Cr_1 gets more even. Based
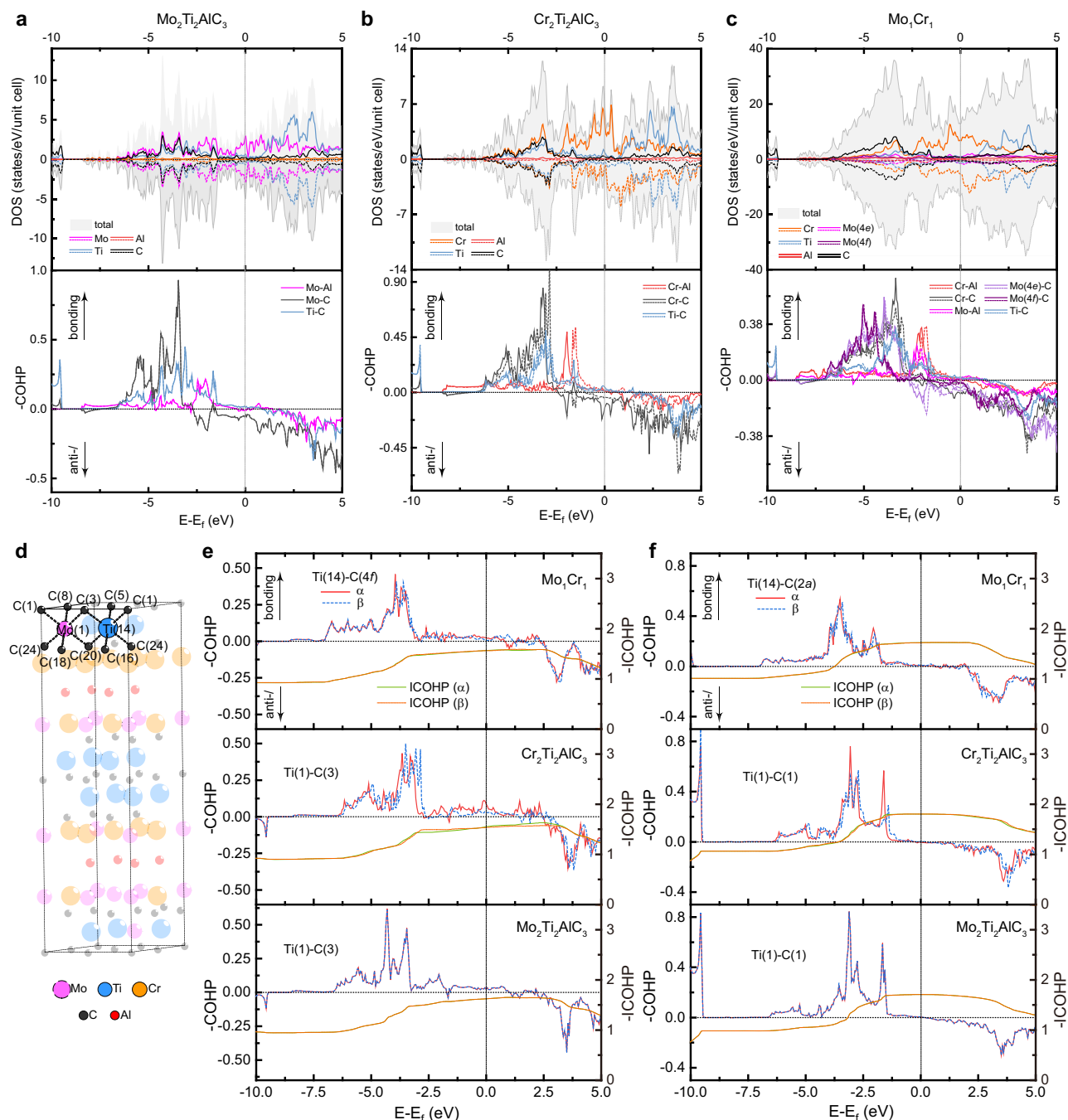
Fig. 4 | Electronic structure and bonding analysis. a–c Total density of states (TDOS) and corresponding negative average crystal orbital Hamilton population ($-$COHP) of $Mo_2Ti_2AlC_2$ (**a**), $Cr_2Ti_2AlC_3$ (**b**), and Mo_1Cr_1 (**c**), respectively. **d** Schematic illustration of the coordination environments of Ti(14) atom at $4f$ site with an adjacent Mo(1) atom in Mo_1Cr_1. **e, f** Average $-$COHP and integrated $-$COHP curves ($-$ICOHP) of (**e**) Ti-C($4f$) bonds in Mo_1Cr_1 and the two parental o-MAXs, (**f**) Ti-C($2a$) bonds in Mo_1Cr_1 and the two parental o-MAXs. The $-$COHP curves of each bond are colored in red and blue, whereas the $-$ICOHP curves are colored in green and orange. Solid and dash lines represent the α and β spin, respectively. Source data are provided as a Source Data file.

on the heterodesmic bond nature of the MAX phase, not only the bond strength ratio of M-Al and M-C bonds but also the ratio among different M-C bonds is critical for the sequence of bond breaking[59,60]. Eventually, benefiting from the relatively large bond strength ratio of M-C over the M-Al bond, as well as a more even bond strength distribution in the M_4C_3 layer of Mo_1Cr_1, tunable and enhanced mechanical properties can be expected.

Therefore, the anisotropic elastic properties of $Mo_2Ti_2AlC_3$, $Cr_2Ti_2AlC_3$, and Mo_1Cr_1 were compared by calculating the second order elastic constants c_{ij} (Supplementary Table 10). As summarized,

the Mo_1Cr_1 presents c_{11} and c_{12} in between those of the $Mo_2Ti_2AlC_3$ and $Cr_2Ti_2AlC_3$, while the c_{13}, c_{33}, and c_{44} are higher than both o-MAXs. A stronger bonding along the c-axis than a-axis ($c_{33} > c_{11}$) is observed in Mo_1Cr_1 as well[61,62], which is in agreement with the change in bond strength and strength distribution predicted by $-$ICOHP values (Supplementary Fig. 13). By calculating the linear compressibility coefficients (k_c/k_a) based on the elastic constants[58], M_1Cr_1 presents the largest deviation of k_c/k_a from 1 (0.69 for Mo_1Cr_1, 0.82 for $Cr_2Ti_2AlC_3$, and 1.13 for $Mo_2Ti_2AlC_3$), which implies the highest anisotropic compressibility. Accordingly, based on Hill's average[63], elastic-dependent
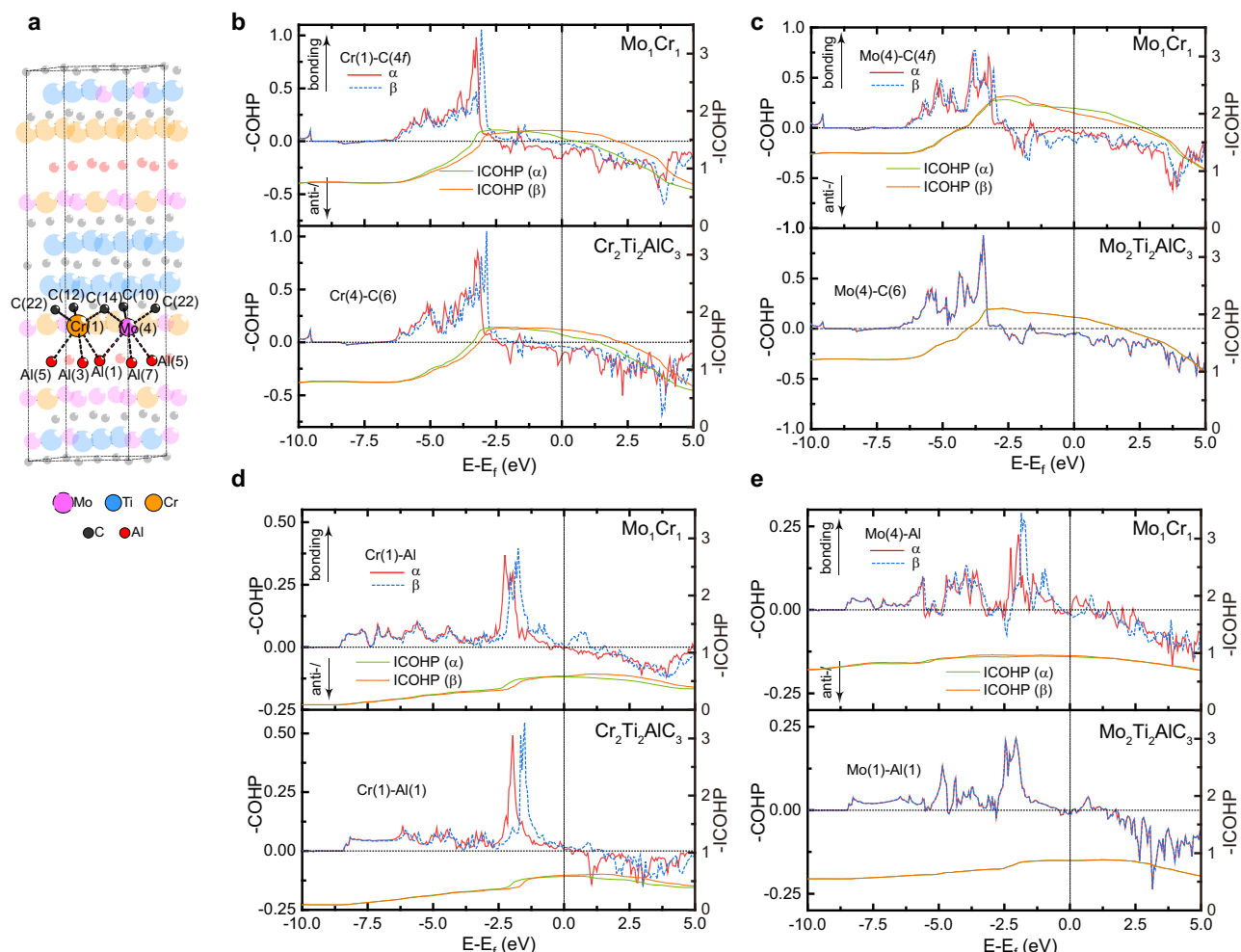
Fig. 5 | Bonding analysis of the 4e metal. a Schematic illustration of the coordination environments of Cr(1) atom at $4e$ site with an adjacent Mo(4) atom. **b–e** Negative average crystal orbital Hamilton population (−COHP) and integrated −COHP curves (−ICOHP) of (**b**) Cr-C($4f$) bonds in Mo_1Cr_1 and $Cr_2Ti_2AlC_3$, (**c**) Mo-C($4f$) bonds in Mo_1Cr_1 and $Mo_2Ti_2AlC_3$, (**d**) Cr-Al bonds in Mo_1Cr_1 and $Cr_2Ti_2AlC_3$, (**e**) Mo-Al bonds in Mo_1Cr_1 and $Mo_2Ti_2AlC_3$. The −COHP curves of each bond are colored in red and blue, whereas the −ICOHP curves are colored in green and orange. Solid and dash lines represent the α and β spin, respectively. Source data are provided as a Source Data file.

properties including bulk modulus (B_H), Young's modulus (E_H), shear modulus (G_H), and Poisson's ratio (ν_H) were calculated as well (Supplementary Table 11). As shown, an increased E_H and G_H, are predicted in the solid solution structure of Mo_1Cr_1, which implies an improved mechanical property.
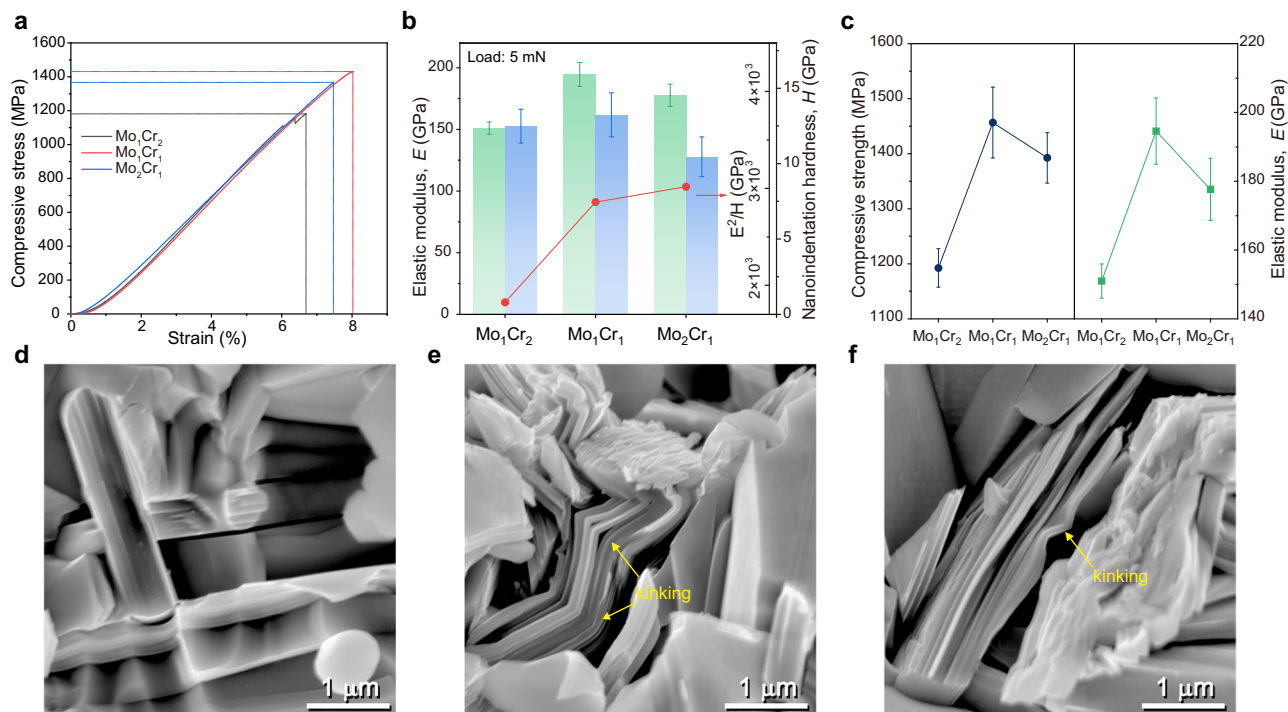
Mechanical properties of the quinary o-MAXs

Under the guidance of theoretical predictions, room-temperature stress-strain curves of the three as-synthesized o-MAXs (Mo_1Cr_2, Mo_1Cr_1, and Mo_2Cr_1) up to failure were recorded and depicted in Fig. 6a and Supplementary Fig. 14. As shown, Mo_1Cr_2 delivers a compressive strength of 1192.5 ± 35.0 at 6.9% strain. Whereas with increasing Mo content, Mo_1Cr_1 and Mo_2Cr_1 present a high compressive strength of 1456.7 ± 64.3 at 7.7% strain and 1392.5 ± 45.7 MPa at 7.7% strain, respectively. In consideration of the similar grain size of the three o-MAXs, the evolution of mechanical properties can be dominated by chemical composition and secondary ordering. Meanwhile, although the corresponding metal carbides and oxides are typical impurities in the synthesized o-MAXs[31,35,64], the impacts of TiC and Al_2O_3 on the mechanical properties of the new MAXs should be excluded. Thus, nanoindentation was applied to the three o-MAXs. The load-displacement curves of annealed samples are plotted in Supplementary Fig. 15. The elastic modulus (E) and nanoindentation hardness

(H) of the three MAXs are calculated based on the Oliver-Pharr model[65,66]. As plotted in Fig. 6b, the Mo_1Cr_1 delivers the highest E and H among the three o-MAXs as well. Meanwhile, the respective ratio of E^2/H that represents the capacity of energy dissipation of each quinary o-MAX is calculated (Fig. 6b)[67,68]. As shown, the E^2/H of Mo_1Cr_1 and Mo_2Cr_1 is nearly 1.5 times higher than that of the Mo_1Cr_2. Figure 6c compares the compressive strength of the three MAXs together with their E. As shown, a coincident trend in both the strength from macroscopic compression and the E from nanoindentation is revealed. Given the consistent performance from both macro and microscopic scales, the obtained compressive strength of the three quinary o-MAXs might not have been affected by the minor amount of impurities and thus is credible and intrinsically comparable. Notably, the compressive strength achieved by Mo_1Cr_1 is not only the highest among the three quinary o-MAXs but also higher than that of the $Mo_2Ti_2AlC_3$ MAX[28], which is in agreement with the theoretical predictions. Meanwhile, such value excels previously reported MAXs[27,28,30,31,33–40,43,44,64,69,70], and is comparable to some common engineering ceramics like alumina as well (Supplementary Table 1)[71–74].

The morphology of surfaces after compression tests from three MAXs was observed under high-magnification SEM (Fig. 6d–f). As shown, the Mo_1Cr_2 delivers distinct undeformed grains on a cracked surface after compression, whereas typical kinking structures are

Fig. 6 | Mechanical properties of the quinary *o*-MAXs. a Typical stress-strain curves of the three *o*-MAXs under a compressive rate of 10^{-3} s^{-1}. **b** The elastic modulus E (in green), nanoindentation hardness H (in blue), and the calculated E^2/H (in red) of the three MAXs with a peak load of 5 mN. **c** Change on the compressive strength (in dark blue) and E (in green) of the three MAXs upon their chemical composition. **d**–**f** High-magnification SEM images show the typical surface morphology after compression tests: Mo$_1$Cr$_2$ (**d**), Mo$_1$Cr$_1$ (**e**), and Mo$_2$Cr$_1$ (**f**), respectively. The yellow arrows indicate the kinking within the grains. The error bars in (**b**) represent the standard deviations from ten parallel measurements, while the error bars of compressive strength in (**c**) represent the standard deviations from five parallel measurements. Source data are provided as a Source Data file.

observed in the grain of Mo$_1$Cr$_1$ and Mo$_2$Cr$_1$. Given the dramatically extended path of crack propagation and enlarged cracking surface by forming kinking in the nanolamellas, a higher capacity of energy dissipation of Mo$_1$Cr$_1$ and Mo$_2$Cr$_1$ is concluded, which is in accordance with their higher E^2/H value.

In summary, a strategy toward new *o*-MAX is demonstrated by forming solid solutions of two existing *o*-MAXs (Cr$_{2.5}$Ti$_{1.5}$AlC$_3$ and Mo$_2$Ti$_2$AlC$_3$), and a miscible chemical ordering is demonstrated. Three quinary *o*-MAXs that inherit the out-of-plane ordering from the parental *o*-MAXs have been obtained. DFT calculations are performed to illuminate the electronic structure and chemical bonding characters of the quinary *o*-MAX, which reveals anisotropic and improved mechanical properties. Accordingly, the theoretically predicted mechanical properties have been verified by both macroscopic compression and nanoindentation tests, where high compressive strength, as well as the tunable capacity of energy dissipation after forming solid solution, is observed in quinary *o*-MAXs. Given the tunability in chemical composition, structural ordering, as well as mechanical properties, the quinary Ti-Cr-Mo *o*-MAXs prove a way towards constructing the chemical complex *o*-MAXs and would enjoy a bright prospect in multiple applications.

Methods

Synthesis of the Ti-Cr-Mo solid solution *o*-MAX

The quinary MAX was synthesized by spark plasma sintering (SPS) the powder mixture at 1500 °C. Briefly, elemental powders of Ti, Cr, and Mo with stoichiometric ratio were ball milled with Al and flake graphite powders. The molar ratio of metal:Al:C was 4:1.2:3, for which an excessed amount of Al was adopted. For the three *o*-MAXs, the typical mass of Ti, Cr, Mo, Al, and C was 2.69 g, 2.92 g, 2.16 g, 1.10 g, 1.22 g for (Cr$_{0.78}$Mo$_{0.22}$)$_2$(Ti$_{0.87}$Mo$_{0.13}$)$_2$AlC$_3$ (Mo$_1$Cr$_2$); 3.04 g, 2.38 g, 3.06 g,

1.18 g, 1.32 g (Cr$_{0.65}$Mo$_{0.35}$)$_2$(Ti$_{0.88}$Mo$_{0.12}$)$_2$AlC$_3$ (Mo$_1$Cr$_1$); and 2.96 g, 1.46 g, 4.32 g, 1.10 g, 1.22 g for (Cr$_{0.52}$Mo$_{0.48}$)$_2$(Ti$_{0.88}$Mo$_{0.12}$)$_2$AlC$_3$ (Mo$_2$Cr$_1$), respectively. A SPEX 8000 M high-energy ball mill with a clamp speed of 875 cycles per minute was utilized for the ball milling. The weighting and milling processes were carried out in an Ar atmosphere. The homogeneous powder mixture was cold pressed in a *h*-BN coated graphite dies (ϕ30 mm) under 30 MPa for 10 min, and then sintered at 1500 °C for 15 min under a uniaxial pressure of 30 MPa in vacuum. The heating and cooling rates were 100 °C min^{-1}.

To achieve a high phase purity, the as-sintered specimens were annealed in a tube furnace at 1500 °C for 2 h under an Ar atmosphere, the heating and cooling rates were no more than 10 °C min^{-1}.

First-principle calculations

Density functional theory (DFT) calculations were performed on Vienna ab initio Simulation Package (VASP) by using the projector augmented-wave (PAW) method[75,76]. The exchange-correlation functional energy was described by generalized gradient approximation (GGA) with Perdew-Burke-Ernzerhof (PBE) scheme[77]. For modeling the structure of two parental *o*-MAXs, a plane-wave cutoff of 600 eV and the $15 \times 15 \times 1$ k-points of the Brillouin zone were used. To simplify the model, the Cr, Mo, and Ti in the Cr-Ti and Mo-Ti binary *o*-MAXs were set to solely occupy the 4*e* and 4*f* Wyckoff sites, i.e., Cr$_2$Ti$_2$AlC$_3$ and Mo$_2$Ti$_2$AlC$_3$. Whereas to simulate the Mo$_1$Cr$_1$, an atomic occupancy with the formula (Cr$_{0.625}$Mo$_{0.375}$)$_2$(Ti$_{0.875}$Mo$_{0.125}$)$_2$AlC$_3$ was taken (Supplementary Data 1). The solid solution of Cr, Mo, and Ti atoms in the structure of Mo$_1$Cr$_1$ was processed by creating random structures using the special quasi-random structure (SQS) method[78]. Accordingly, a $2 \times 2 \times 1$ supercell with a $9 \times 9 \times 1$ k-point mesh was utilized for Mo$_1$Cr$_1$. Spin polarization was adopted in the three models to fulfill the requirement of magnetic configuration in two Cr-contained *o*-MAXs

and keep consistency in $Mo_2Ti_2AlC_3$. The relaxation of atomic geometries was achieved using the conjugate-gradient method. The maximum force tolerance of $0.02\,eV\,Å^{-1}$ and a convergence precision of $1.0 \times 10^{-5}\,eV\,atom^{-1}$ was taken as the criteria for geometry optimization. Chemical bonding analyses of plane-wave data were performed based on a variant of the crystal orbital Hamilton population ($-COHP$) technique by using the Local-Orbital Basis Suite Towards Electronic-Structure Reconstruction software package (LOBSTER-5.1.1[53,54,79,80]).

The elastic constants of the three structures were determined based on an energy-strain method, during which the structures after applying strain were generated by VASPKIT in batches[81]. For calculating the elastic constants, $21 \times 21 \times 2$ k-points for the two parental o-MAXs and $12 \times 12 \times 2$ k-points for Mo_1Cr_1 were adopted. Seven distorted structures were used to calculate the elastic constant, in which the lattice deformations δ ranged from -0.015 to 0.015 with a step size of 0.005. After calculating the energy of each deformed structure, the elastic constant of the material is calculated by binomial fitting.

Mechanical properties

All sintered disks were polished by SiC paper sequentially to 2000-grit, and then cleaned with ethanol before the following tests.

Nanoindentation test was executed at a peak load of 5 mN (Hysitron, Bruker), the loading and unloading time were 5 s, whereas the dwell time was 2 s. At least 10 indentations were performed for each sample to determine the elastic modulus (E) and nanoindentation hardness (H).

Compressive tests were performed using cylindrical-shaped specimens ($\phi 5.0\,mm$ and 8 mm in height). Samples were machined by electro-discharging and polished by SiC paper before test. Compressive tests were performed in the air using an electromechanical universal testing machine (MTS 5105, China) with a maximum load of 100-kN, supplied with a controller that allowed tests to be run either in displacement or load control mode. In all tests, a preload of 1–2 MPa that corresponded to stress, s, was applied to keep the samples aligned. The obtained the mean and standard deviation (SD) of the samples, at least 5 specimens were tested for each MAXs.

Materials characterizations

All the X-ray diffraction (XRD) patterns were collected on a Bruker D8 ADVANCE diffractometer, with a 2θ range of 5–120° and a scan step of 0.02°. The lattice parameter and phase purity of the specimens were analyzed via Rietveld refinements using GSAS II software.[82] For refining the atomic occupation of Ti, Mo, and Cr in the $4f$ and $4e$ Wyckoff sites, atoms that potentially co-occupation were assigned at the same coordinate position, and constrained by the same atomic parameters to be the equivalent atoms. During the following refinement, unstable combinations (abnormal in position and atomic fraction) were removed to obtain the most possible one. High-angle annular dark-field (HAADF) scanning transmission electron microscopy (STEM) with atomic resolution was utilized to verify the distribution of Ti, Cr, Mo, and Al atoms in the lattice. The HAADF-STEM images were collected on an FEI Themis Z (double Cs correction) transmission electron microscope (TEM). A thin-foil sample for HAADF-STEM was prepared on an FEI Helios G4 CX dual-beam focused ion beam/scanning electron microscope (FIB/SEM). Based on the HAADF-STEM characterizations, energy-dispersive X-ray spectroscopy (EDS) mapping and line profiling were performed as well. The worn and unworn surfaces of the specimens were studied by the SEM, whereas the elemental distribution of the surface was characterized by EDS mapping as well. The density of the sintered specimens was evaluated through Archimedes' method.

Data availability

All data are available in the main text or the supplementary information. Source data are provided with this paper.

References

1. Ma, C. et al. Atomic level out-diffusion and interfacial reactions of MAX phases in contact with metals and air. *J. Eur. Ceram. Soc.* **44**, 1–22 (2024).
2. Tan, Q. et al. Recent progress in additive manufacturing of bulk MAX phase components: A review. *J. Mater. Sci. Technol.* **131**, 30–47 (2022).
3. Zhang, Z. et al. On the formation mechanisms and properties of MAX phases: A review. *J. Eur. Ceram. Soc.* **41**, 3851–3878 (2021).
4. Kubitza, N. et al. Extending the chemistry of layered solids and nanosheets: chemistry and structure of MAX phases, MAB phases and MXenes. *Chem. Plus Chem.* **88**, e202300214 (2023).
5. Yu, H. et al. Mapping the structure and chemical composition of MAX phase ceramics for their high-temperature tribological behaviors. *Carbon Energy* **6**, e597 (2024).
6. Sokol, M. et al. On the chemical diversity of the MAX phases. *Trends Chem.* **1**, 210–223 (2019).
7. Barsoum, M. W. et al. Elastic and mechanical properties of the MAX phases. *Annu. Rev. Mater. Res.* **41**, 195–227 (2011).
8. Guo, L. et al. Effects of pellet surface roughness and pre-oxidation temperature on CMAS corrosion behavior of Ti_2AlC. *J. Adv. Ceram.* **11**, 945–960 (2022).
9. Magnus, C. et al. Synthesis and high temperature corrosion behaviour of nearly monolithic Ti_3AlC_2 MAX phase in molten chloride salt. *Corros. Sci.* **182**, 109193 (2021).
10. Xue, Y. et al. Ordered metal substitution in Ti_3AlC_2 and the effect on tribological behaviors in a wide temperature range. *Tribol. Int.* **178**, 108009 (2023).
11. Du, C.-F. et al. Synthesis of a high-entropy $(TiVCrMo)_3AlC_2$ MAX and its tribological properties in a wide temperature range. *J. Eur. Ceram. Soc.* **43**, 4684–4695 (2023).
12. Wyatt, B. C. et al. Ultra-high temperature ceramics for extreme environments. *Nat. Rev. Mater.* **9**, 773–789 (2024).
13. Eklund, P. et al. Layered ternary $M_{n+1}AX_n$ phases and their 2D derivative MXene: an overview from a thin-film perspective. *J. Phys. D: Appl. Phys.* **50**, 113001 (2017).
14. Hu, W. et al. Layered ternary MAX phases and their MX particulate derivative reinforced metal matrix composite: A review. *J. Alloy. Compd.* **856**, 157313 (2021).
15. Anasori, B. et al. MXenes: trends, growth, and future directions. *Graphene 2D Mater.* **7**, 75–79 (2022).
16. Du, C.-F. et al. Exploring the oxidation behaviors of the Ti-V-Cr-Mo high-entropy MAX at 800 °C for its self-lubricity. *J. Mater. Sci. Technol.* **187**, 49–62 (2024).
17. Chen, L. et al. Two-Dimensional MXenes Derived from Medium/High-Entropy MAX Phases M_2GaC (M = Ti/V/Nb/Ta/Mo) and their Electrochemical Performance. *Small Methods* **7**, 2300054 (2023).
18. Yang, J. et al. Novel W-based in-plane chemically ordered $(W_{2/3}R_{1/3})_2AlC$ (R = Gd, Tb, Dy, Ho, Er, Tm and Lu) MAX phases and their 2D $W_{1.33}C$ MXene derivatives. *Carbon* **183**, 76–83 (2021).
19. Chen, Z. et al. Synthesis and characterizations of solid-solution i-MAX phase $(W_{1/3}Mo_{1/3}R_{1/3})_2AlC$ (R = Gd, Tb, Dy, Ho, Er and Y) and derivated i-MXene with improved electrochemical properties. *Scr. Mater.* **213**, 114596 (2022).
20. Dahlqvist, M. et al. Origin of Chemically Ordered Atomic Laminates (i-MAX): Expanding the Elemental Space by a Theoretical/Experimental Approach. *ACS Nano* **12**, 7761–7770 (2018).
21. Dahlqvist, M. et al. Predictive theoretical screening of phase stability for chemical order and disorder in quaternary 312 and 413 MAX phases. *Nanoscale* **12**, 785–794 (2020).
22. Dahlqvist, M. et al. Order and disorder in quaternary atomic laminates from first-principles calculations. *Phys. Chem. Chem. Phys.* **17**, 31810–31821 (2015).
23. Dahlqvist, M. et al. MAX phases – Past, present, and future. *Mater. Today* **72**, 1–24 (2024).

24. Wyatt, B. C. et al. Design of Atomic Ordering in $Mo_2Nb_2C_3T_x$ MXenes for Hydrogen Evolution Electrocatalysis. *Nano Lett.* **23**, 931–938 (2023).

25. Tao, Q. et al. Thin film synthesis and characterization of a chemically ordered magnetic nanolaminate $(V,Mn)_3GaC_2$. *APL Mater.* **4**, 086109 (2016).

26. Xue, Y. et al. Transformation of chemical ordering and configuration entropy in quaternary $Cr_xTi_{0.75}Mo_{0.75}V_{1.5-x}AlC_2$ MAXs system. *J. Adv. Ceram.* **13**, 1861–1871 (2024).

27. Niu, Y. et al. Synthesis, microstructure, and properties of high purity Mo_2TiAlC_2 ceramics fabricated by spark plasma sintering. *J. Adv. Ceram.* **9**, 759–768 (2020).

28. Fu, S. et al. Synthesis and characterization of high purity $Mo_2Ti_2AlC_3$ ceramic. *J. Alloy. Compd.* **815**, 152485 (2020).

29. Ritchie, R. O. The conflicts between strength and toughness. *Nat. Mater.* **10**, 817–822 (2011).

30. El-Raghy, T. et al. Damage Mechanisms around Hardness Indentations in Ti_3SiC_2. *J. Am. Ceram. Soc.* **80**, 513–516 (1997).

31. Barsoum, M. W. et al. Processing and characterization of Ti_2AlC, Ti_2AlN, and $Ti_2AlC_{0.5}N_{0.5}$. *Metall. Mater. Trans. A* **31**, 1857–1865 (2000).

32. Salama, I. et al. Synthesis and mechanical properties of Nb_2AlC and $(Ti,Nb)_2AlC$. *J. Alloy. Compd.* **347**, 271–278 (2002).

33. Wang, X. H. et al. Microstructure and properties of Ti_3AlC_2 prepared by the solid–liquid reaction synthesis and simultaneous in-situ hot pressing process. *Acta Mater.* **50**, 3143–3151 (2002).

34. Zhou, Y. C. et al. Strengthening of Ti_3AlC_2 by incorporation of Si to form $Ti_3Al_{1-x}Si_xC_2$ solid solutions. *Acta Mater.* **54**, 1317–1322 (2006).

35. Amini, S. et al. Synthesis and mechanical properties of fully dense Ti_2SC. *J. Am. Ceram. Soc.* **90**, 3953–3958 (2007).

36. Hu, C. et al. Physical and Mechanical Properties of Bulk Ta_4AlC_3 Ceramic Prepared by an In Situ Reaction Synthesis/Hot-Pressing Method. *J. Am. Ceram. Soc.* **90**, 2542–2548 (2007).

37. Hu, C. et al. In situ reaction synthesis and mechanical properties of V_2AlC. *J. Am. Ceram. Soc.* **91**, 4029–4035 (2008).

38. Hu, C. et al. Microstructure and properties of bulk Ta_2AlC ceramic synthesized by an in situ reaction/hot pressing method. *J. Eur. Ceram. Soc.* **28**, 1679–1685 (2008).

39. Hu, C. et al. In Situ Reaction Synthesis, Electrical and Thermal, and Mechanical Properties of Nb_4AlC_3. *J. Am. Ceram. Soc.* **91**, 2258–2263 (2008).

40. Ying, G. et al. Synthesis and mechanical properties of high-purity Cr_2AlC ceramic. *Mater. Sci. Eng. A* **528**, 2635–2640 (2011).

41. Cai, L. P. et al. The synthesis and mechanical properties of high pure $Ti_2Al(Sn)C$ solid solution. *Int. J. Appl. Ceram. Technol.* **15**, 1212–1221 (2018).

42. Wo, S. et al. High strengthening effects and excellent wear resistance of $Ti_3Al(Si)C_2$ solid solutions. *Int. J. Appl. Ceram. Technol.* **16**, 2398–2408 (2019).

43. Liu, Z. M. et al. In-situ reaction synthesis and mechanical properties of quaternary MAX phase $(Cr_{2/3}Ti_{1/3})_3AlC_2$. *Ceram. Int.* **46**, 22854–22860 (2020).

44. Cao, L. et al. Synthesis and characterization of high entropy $(TiVNbTaM)_2AlC$ (M = Zr, Hf) ceramics. *J. Adv. Ceram.* **13**, 237–246 (2024).

45. Wang, F. et al. Irradiation damage in $(Zr_{0.25}Ta_{0.25}Nb_{0.25}Ti_{0.25})C$ high-entropy carbide ceramics. *Acta Mater.* **195**, 739–749 (2020).

46. Du, C.-F. et al. Mo-doped Cr-Ti-Mo ternary o-MAX with ultra-low wear at elevated temperatures. *J. Eur. Ceram. Soc.* **42**, 7403–7413 (2022).

47. Anasori, B. et al. Experimental and theoretical characterization of ordered MAX phases Mo_2TiAlC_2 and $Mo_2Ti_2AlC_3$. *J. Appl. Phys.* **118**, 094304 (2015).

48. Liu, Z. et al. $(Cr_{2/3}Ti_{1/3})_3AlC_2$ and $(Cr_{5/8}Ti_{3/8})_4AlC_3$: new MAX-phase compounds in Ti–Cr–Al–C system. *J. Am. Ceram. Soc* **97**, 67–69 (2014).

49. Susi, T. et al. Quantifying transmission electron microscopy irradiation effects using two-dimensional materials. *Nat. Rev. Phys.* **1**, 397–405 (2019).

50. Zhao, S. et al. Phase transformation and amorphization resistance in high-entropy MAX phase M_2SnC (M = Ti, V, Nb, Zr, Hf) under in-situ ion irradiation. *Acta Mater.* **238**, 118222 (2022).

51. Jhi, S.-H. et al. Electronic mechanism of hardness enhancement in transition-metal carbonitrides. *Nature* **399**, 132–134 (1999).

52. Wang, J. Y. et al. Ab initio elastic stiffness of nano-laminate $(M_xM'_{2-x})AlC$ (M and M'= Ti, V and Cr) solid solution. *J. Phys.: Condens. Matter* **16**, 2819–2827 (2004).

53. Dronskowski, R. et al. Crystal orbital Hamilton populations (COHP): energy-resolved visualization of chemical bonding in solids based on density-functional calculations. *J. Phys. Chem.* **97**, 8617–8624 (1993).

54. Deringer, V. L. et al. Crystal Orbital Hamilton Population (COHP) Analysis As Projected from Plane-Wave Basis Sets. *J. Phys. Chem. A* **115**, 5461–5466 (2011).

55. Nelson, R. et al. LOBSTER: Local orbital projections, atomic charges, and chemical-bonding analysis from projector-augmented-wave-based density-functional theory. *J. Comput. Chem.* **41**, 1931–1940 (2020).

56. Qureshi, M. W. et al. Ab initio predictions of structure and physical properties of the Zr_2GaC and Hf_2GaC MAX phases under pressure. *Sci. Rep.* **11**, 3260 (2021).

57. Yu, M. et al. Accurate and efficient algorithm for Bader charge integration. *J. Chem. Phys.* **134**, 064111 (2011).

58. Sailuam, W. et al. A first principles investigation on the structural, elastic, and mechanical properties of MAX phase M_3AlC_2 (M= Ta, Ti, V) as a function of pressure. *Computational Condens. Matter* **30**, e00638 (2022).

59. Zhou, J. et al. Boridene: Two-dimensional $Mo_{4/3}B_{2-x}$ with ordered metal vacancies obtained by chemical exfoliation. *Science* **373**, 801–805 (2021).

60. Bai, Y. L. et al. Density Functional Theory Study of $M_{n+1}AXn$ Phases: A Review. *Crit. Rev. Solid State Mater. Sci.* **44**, 56–107 (2019).

61. Fu, H. et al. Structural, elastic and thermodynamic properties of $Ti2SC$. *Bull. Mater. Sci.* **34**, 1617–1625 (2011).

62. Sultana, F. et al. First principles study of M_2InC (M=Zr, Hf and Ta) MAX phases. The effect of M atomic species. *Results Phys.* **11**, 869–876 (2018).

63. Hill, R. The Elastic Behaviour of a Crystalline Aggregate. *Proc. Phys. Soc. A* **65**, 349 (1952).

64. Ganguly, A. et al. Synthesis and mechanical properties of Ti_3GeC_2 and $Ti_3(Si_xGe_{1-x})C2$ (x = 0.5, 0.75) solid solutions. *J. Alloy. Compd.* **376**, 287–295 (2004).

65. Oliver, W. C. et al. An improved technique for determining hardness and elastic modulus using load and displacement sensing indentation experiments. *J. Mater. Res.* **7**, 1564–1583 (1992).

66. Yang, S. et al. TEM-MD characterization of KDP deformation mechanisms under nanoindentation. *J. Eur. Ceram. Soc.* **43**, 3844–3848 (2023).

67. Leyland, A. et al. On the significance of the H/E ratio in wear control: a nanocomposite coating approach to optimised tribological behaviour. *Wear* **246**, 1–11 (2000).

68. Bao, Y. W. et al. Investigation of the relationship between elastic modulus and hardness based on depth-sensing indentation measurements. *Acta Mater.* **52**, 5397–5404 (2004).

69. Barsoum, M. W. et al. Characterization of Ti_4AlN_3. *Metall. Mater. Trans. A* **31**, 333–337 (2000).

70. Amini, S. et al. Synthesis and elastic and mechanical properties of Cr_2GeC. *J. Mater. Res.* **23**, 2157–2165 (2008).

71. Gautam, C. et al. Zirconia based dental ceramics: structure, mechanical properties, biocompatibility and applications. *Dalton Trans.* **45**, 19194–19215 (2016).

72. Zhang, Q. et al. Explosive fragmentations of alumina (Al$_2$O$_3$) under quasistatic compressive loading. *EPJ Web Conf.* **94**, 01056 (2015).

73. Peters, A. B. et al. Reactive two-step additive manufacturing of ultra-high temperature carbide ceramics. *Addit. Manuf.* **61**, 103318 (2023).

74. Zeng, X. et al. Mechanical properties and biological activity of 3D printed silicon nitride materials. *Ceram. Int.* **50**, 16704–16713 (2024).

75. Vanderbilt, D. Soft self-consistent pseudopotentials in a generalized eigenvalue formalism. *Phys. Rev. B* **41**, 7892–7895 (1990).

76. Clark, S. J. et al. First principles methods using CASTEP. *Z. Kristallogr. Cryst. Mater.* **220**, 567–570 (2005).

77. Perdew, J. P. et al. Pair-distribution function and its coupling-constant average for the spin-polarized electron gas. *Phys. Rev. B* **46**, 12947–12954 (1992).

78. Zunger, A. et al. Special quasirandom structures. *Phys. Rev. Lett.* **65**, 353–356 (1990).

79. Maintz, S. et al. Analytic projection from plane-wave and PAW wavefunctions and application to chemical-bonding analysis in solids. *J. Comput. Chem.* **34**, 2557–2567 (2013).

80. Maintz, S. et al. LOBSTER: A tool to extract chemical bonding from plane-wave based DFT. *J. Comput. Chem.* **37**, 1030–1035 (2016).

81. Wang, V. et al. VASPKIT: A user-friendly interface facilitating high-throughput computing and analysis using VASP code. *Comput. Phys. Commun.* **267**, 108033 (2021).

82. Toby, B. H. et al. GSAS-II: the genesis of a modern open-source all purpose crystallography software package. *J. Appl. Crystallogr.* **46**, 544–549 (2013).

Acknowledgements

Author contributions

C.D. and H.Y. conceived and coordinated all stages of this research. C.W. and Y.X. carried out the experiments. M.X. and W.Q. performed the DFT calculation. L.X. and C.M. performed the characterization. L.W. and X.L. provided resources and instrumentations. C.W., C.D., and H.Y. wrote the paper. All authors discussed the results and revised the paper.

Competing interests

The authors declare no competing interests.

Additional information

Correspondence and requests for materials should be addressed to Cheng-Feng Du, Weihong Qi or Hong Yu.

Peer review information *Nature Communications* thanks the anonymous reviewer(s) for their contribution to the peer review of this work. A peer review file is available.

Reprints and permissions information is available at http://www.nature.com/reprints

Publisher's note Springer Nature remains neutral with regard to jurisdictional claims in published maps and institutional affiliations.